Time-dependent Tonks-Langmuir model is unstable

T. E. Sheridan*
Department of Physics and Astronomy, Ohio Northern University, Ada, Ohio 45810 USA

S. D. Baalrud†
Department of Physics and Astronomy, University of Iowa, Iowa City, Iowa 52242 USA

(Received 25 July 2017; published 7 November 2017)

We investigate a time-dependent extension of the Tonks-Langmuir model for a one-dimensional plasma discharge with collisionless kinetic ions and Boltzmann electrons. Ions are created uniformly throughout the volume and flow from the center of the discharge to the boundary wall due to a self-consistent, zero-order electric field. Solving this model using a particle-in-cell simulation, we observe coherent low-frequency, long-wavelength unstable ion waves which move toward the boundary with a speed below both the ion acoustic speed and the average ion velocity. The maximum amplitude of the wave potential fluctuations peaks at $\approx 0.09 T_e$ near the wall, where T_e is the electron temperature in electron volts. Using linear kinetic theory, we identify this instability as slow ion-acoustic wave modes which are destabilized by the zero-order electric field.

DOI: 10.1103/PhysRevE.96.053201

I. INTRODUCTION

The Tonks-Langmuir (TL) model [1] is a seminal theory for the low-pressure discharge and the plasma-sheath transition region [2–4] which predicts the time-independent ion velocity distribution function, plasma density, and electrostatic potential profile spanning the plasma and sheath. The TL model is an open system wherein ions are created *ex nihilo*, leading to the establishment of a zero-order electric field which accelerates ions to the walls. The TL model has played a major role in our understanding of plasma discharges and aided in advancing modeling in plasma materials processing, diagnostics, lighting, plasma-spacecraft interactions, and many more applications. It has been tested experimentally [5–8] and several extensions have been developed to more accurately model certain discharges including different models for sourcing the ions [9–12], asymmetric discharges [13], collisional plasmas [14], finite source temperature [15–17], different electron models [18,19], and electronegative discharges [20].

The TL model is a steady-state model (i.e., $\partial/\partial t = 0$, where t is time), but recent work has shown that microinstabilities driven by the relative drift between ions and electrons [21,22], or different ion species [23,24], can arise in low-pressure discharges and may significantly influence transport via wave-particle scattering [25]. It is natural to question if microinstabilities arise in a time-dependent Tonks-Langmuir model [15], and, if so, to what extent they might modify the steady-state solutions. Recent work has suggested that the Tonks-Langmuir model may be susceptible to instabilities, and potential oscillations near the ion plasma frequency have been observed in particle-in-cell simulations [26]. Generic ion-acoustic instabilities have been invoked to explain experimentally measured anomalous thermalization of ions near the sheath edge [22].

In this work we report a low-frequency instability in a time-dependent extension of the Tonks-Langmuir model. The model consists of the time-dependent ion Vlasov equation with an ion source and Boltzmann electrons which are coupled through the plasma potential by Poisson's equation. Direct numerical solutions reveal long-wavelength unstable acoustic waves which are excited near the center of the discharge and move with speeds well below the ion acoustic speed. The instability, which is driven by the zero-order electric field, is fundamentally different than the standard ion-acoustic-type instability which is driven by the relative drift between ions and kinetic electrons. In fact, standard ion-acoustic instabilities are not possible in this model because the electron density is solved via the Boltzmann density relation, precluding inverse electron Landau damping, which is the mechanism by which the standard ion-acoustic instability grows.

Although essential features of the observed instabilities are nonlinear, linearization of the time-dependent TL model equations reveals the mechanism responsible for their excitation. In particular, slow ion-acoustic waves are excited directly by the zero-order electric field as predicted by the linear dispersion relation and first introduced by Fried *et al.* [27]. These waves, which are convected to the wall by the ion flow, are fundamentally different than standard ion-acoustic instabilities because they are driven directly by the free energy in the zero-order electric field, rather than by a differential flow, and are present even in the absence of a differential flow.

This paper is organized as follows. Section II describes the time-dependent extension of the TL model. In Sec. III we present numerical solutions of the model and demonstrate the existence of unstable acoustic modes. Section IV describes the linear theory both for a general steady-state ion velocity distribution function (IVDF) and for a Maxwellian IVDF. Results from the linear theory are given in Sec. V and show that the theory predicts an unstable wave whose features match the instability observed in the simulation. Conclusions are presented in Sec. VI.

II. THE TONKS-LANGMUIR MODEL

In the TL model [1] a plasma with a single positive ion species with ion charge e and mass M and Boltzmann electrons

*t-sheridan@onu.edu
†scott-baalrud@uiowa.edu

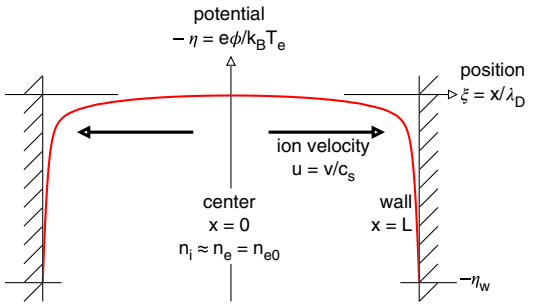

FIG. 1. Schematic of the Tonks-Langmuir discharge model. Cold ions are created and then accelerated to the walls by the self-consistent electric field.

is created in the region between two large flat, perfectly absorbing electrodes (i.e., walls). The system is assumed to have a one-dimensional slab geometry, where $x = 0$ at the center of the discharge (Fig. 1). A steady-state, self-consistent potential $\phi(x)$ is established between the walls. Ions are born at rest (i.e., cold) and are accelerated to the walls by the self-consistent electric field, creating a non-Maxwellian ion distribution function $f(x,v)$, where v is the ion velocity. Electrons are assumed to be in thermal equilibrium with a temperature T_e. The rate of ion creation may be either uniform or proportional to the electron density [2]. We consider the case of a uniform ion source, which may be due to a small component of high-energy electrons [15], e.g., a multidipole confined filament discharge.

The steady-state TL model can be formulated as follows. The ion distribution function $f(x,v)$ is a self-consistent solution of a time-independent Vlasov equation:

$$v\frac{\partial f}{\partial x} + \frac{eE}{M}\frac{\partial f}{\partial v} = S(x,v), \tag{1}$$

where $E = -d\phi/dx$ and $S(x,v)$ is the ion source term. The ion number density is related to $f(x,v)$

$$n_i(x) = \int f(x,v)dv \tag{2}$$

and the electron density is given by the Boltzmann relation

$$n_e = n_{e0}\exp\left(\frac{e\phi}{k_BT_e}\right), \tag{3}$$

where k_B is Boltzmann's constant and n_{e0} is the electron density for $\phi = 0$, which is typically at the center of the discharge $x = 0$. The electron and ion densities are linked through the self-consistent potential ϕ by Poisson's equation

$$\frac{d^2\phi}{dx^2} = -\frac{e}{\epsilon_0}(n_i - n_e), \tag{4}$$

where ϵ_0 is the permittivity of free space. Boundary conditions are $\phi = 0$ at the center of the discharge (so $n_e = n_{e0} \approx n_i$) and $\phi = \phi_w < 0$ at the wall $x = L$. For the TL model with ions born at rest and a spatially uniform source,

$$S(x,v) = \nu n_{e0}\delta(v), \tag{5}$$

where ν is a creation rate of ions per unit time and $\delta(v)$ is the Dirac δ function. Equations (1)–(5) make up the time-independent TL model.

This model can be recast as a single integrodifferential equation [1,2,4] for $\phi(x)$. In particular, the Vlasov equation is solved using the method of characteristics to give an expression for the ion density at a position where the potential is $\phi(x)$,

$$n_i(x) = \sqrt{\frac{M}{2e}}\int_0^x \frac{\nu n_{e0}dx'}{\sqrt{\phi(x') - \phi(x)}}, \tag{6}$$

which can be substituted into Poisson's equation to give the full plasma sheath equation [4]

$$\frac{d^2\phi}{dx^2} = -\frac{e}{\epsilon_0}\left[\sqrt{\frac{M}{2e}}\int_0^x \frac{\nu n_{e0}dx'}{\sqrt{\phi(x') - \phi(x)}} - n_{e0}\exp\left(\frac{e\phi}{k_BT_e}\right)\right]. \tag{7}$$

This equation is nondimensionalized using

$$\eta = -\frac{e\phi}{k_BT_e}, \quad \zeta = \frac{x}{L_\nu}, \quad L_\nu = \frac{\sqrt{2}}{\nu}\sqrt{\frac{k_BT_e}{M}},$$
$$\lambda_D = \sqrt{\frac{\epsilon_0 k_BT_e}{e^2 n_{e0}}}, \tag{8}$$

where L_ν is called the ionization length and λ_D is the electron Debye length at the center of the discharge. The dimensionless plasma sheath equation is

$$\frac{\lambda_D^2}{L_\nu^2}\frac{d^2\eta}{d\zeta^2} = \int_0^\xi \frac{d\zeta'}{\sqrt{\eta(\zeta) - \eta(\zeta')}} - e^{-\eta}. \tag{9}$$

Solutions depend on a single parameter—the squared ratio of the Debye length to the ionization length. For the system to be a plasma $\lambda_D \ll L_\nu$ and in the plasma approximation (strict charge neutrality) $\lambda_D/L_\nu = 0$. Plasma solutions are effectively independent of λ_D/L_ν for $\lambda_D/L_\nu \ll 1$ and then the only length scale is L_ν. Exact analytic solutions are known in the plasma approximation [2,4].

To build a time-dependent TL model we need only replace Eq. (1) with the time-dependent ion Vlasov equation

$$\frac{\partial f}{\partial t} + v\frac{\partial f}{\partial x} + \frac{eE}{M}\frac{\partial f}{\partial v} = S(x,v), \tag{10}$$

while Poisson's equation [Eq. (4)] is unchanged. The model now includes standard ion-acoustic waves with an ion acoustic speed given by

$$c_s = \sqrt{\frac{k_BT_e}{M}} \tag{11}$$

and ion plasma oscillations with a frequency given by

$$\omega_{\rm pi} = \sqrt{\frac{n_{e0}e^2}{\epsilon_0 M}}, \tag{12}$$

where $\lambda_D = c_s/\omega_{\rm pi}$. Since electrons are assumed massless, the time-dependent TL model does not include electron waves or electron Landau damping.

III. TIME-DEPENDENT SOLUTIONS

We use a particle-in-cell (PIC) code to compute solutions of the time-dependent TL model, where the trajectories of the ion particles are the characteristic curves of the ion Vlasov equation [Eq. (10)]. Even though the time-independent system

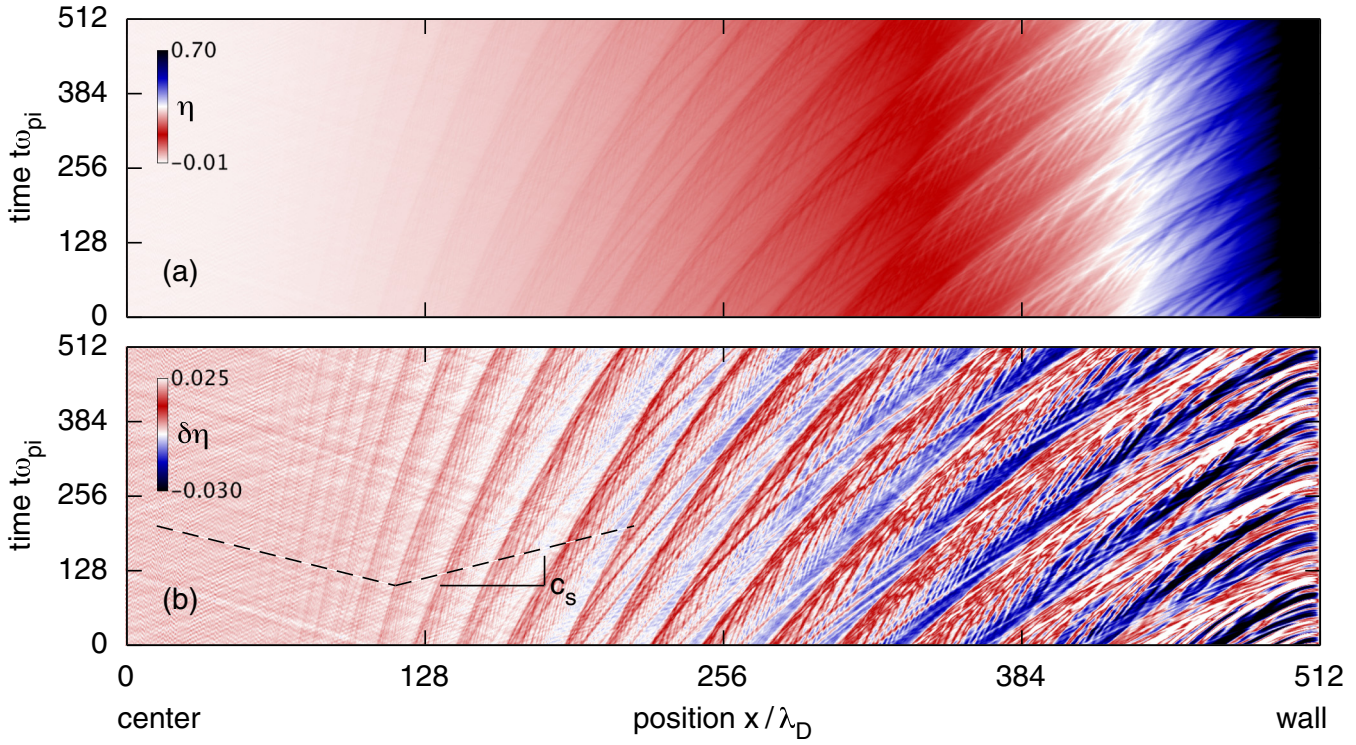

FIG. 2. Steady-state space-time plots of (a) the dimensionless potential $\eta = -e\phi/kT_e$ and (b) the potential fluctuations $\delta\eta(x,t) = \eta(x,t) - \langle\eta\rangle(x)$ computed by subtracting the time-averaged potential. The dashed lines in panel (b) show the ion acoustic speed c_s [Eq. (11)]. Standard ion-acoustic waves are visible near the center of the discharge with the speed c_s, while the long-wavelength fluctuations move with a speed well below c_s.

has symmetry around $x = 0$, we simulate the entire system from wall to wall, $x = -L$ to $x = +L$. The ion source rate ν, which is an eigenvalue of the TL model [4], is adjusted until the time-averaged potential at the center of the discharge is approximately zero. Simulation parameters are as follows: grid spacing, $\Delta x = (1/4)\lambda_D$; time step, $\Delta t = (1/16)\omega_{\rm pi}^{-1}$; and wall potential, $\phi_w = -5k_BT_e/e$. The grid is $4096\Delta x$ in extent, so that the total system length is $1024\lambda_D$ and the distance from the center of the simulation box to the wall is $512\lambda_D$. Simulations are run to a final time of $t_f = 7000\omega_{\rm pi}^{-1}$, which is well into the steady-state regime. Ion particles are added uniformly in space using a "quiet start" method [28], and 1024 ions in a simulation cell corresponds to the density n_{e0}. We add 258 ion particles per Δt. In the steady state the simulation contains 3.6×10^6 ion particles.

Space-time plots of the dimensionless potential η [Fig. 2(a)] display the expected background of standard ion-acoustic waves and ion plasma oscillations together with slow acoustic waves. To emphasize the fluctuations, we subtract the time-averaged potential $\langle\eta\rangle$ to give $\delta\eta = \eta - \langle\eta\rangle$ as shown in Fig. 2(b). Ion acoustic waves with a phase velocity c_s [Eq. (11)] are observed near the center of the discharge propagating in both the positive and negative directions. These waves originate near the plasma-sheath boundary and propagate back into the system. In addition to standard ion-acoustic waves which propagate at c_s, there are long-wavelength, large-amplitude acoustic waves that originate near the center of the discharge and move to the walls with speeds well below c_s. Near the center of the discharge, where the instability is first discernible, the wavelength is $\sim 7\lambda_D$–$10\lambda_D$ and increases to $\sim 40\lambda_D$–$50\lambda_D$ near the edge of the discharge due to the increasing wave speed. The paths of the perturbations are roughly parabolic in time so that their velocity (in the laboratory frame) increases with the distance from the center of the discharge.

The power spectral density (psd) of the potential fluctuations $\delta\eta$ as a function of distance x from the center of the discharge averaged over a time interval $1024\omega_{\rm pi}^{-1}$ is shown in Fig. 3. The power is dominated by the slow acoustic modes. A narrow peak is seen in the psd at $\omega = 0.048\omega_{\rm pi}$, which grows with the increasing distance from the center of the discharge. This verifies the existence of a quasicoherent low-frequency unstable acoustic wave which originates near (but not at) the center of the discharge. Several additional higher-frequency modes with lower powers are also visible. Closer to the wall, the instability shows evidence for saturation due to increased power in higher-frequency modes, where the energy in the higher-frequency modes becomes comparable to the energy in the lowest-frequency mode.

The effect of the instability on the ion distribution function $f(x,v)$ is shown in Fig. 4. In Fig. 4(a) we average over a time interval $13\omega_{\rm pi}^{-1}$, which is about one-tenth of the instability period. This reflects the instantaneous effect of the instability on the ion phase-space. As seen previously in the potential fluctuations, the instability begins to grow near the center of the discharge and the wavelength increases with the wave speed as we move toward the wall. In addition, long-wavelength features are modulated by shorter wavelengths corresponding

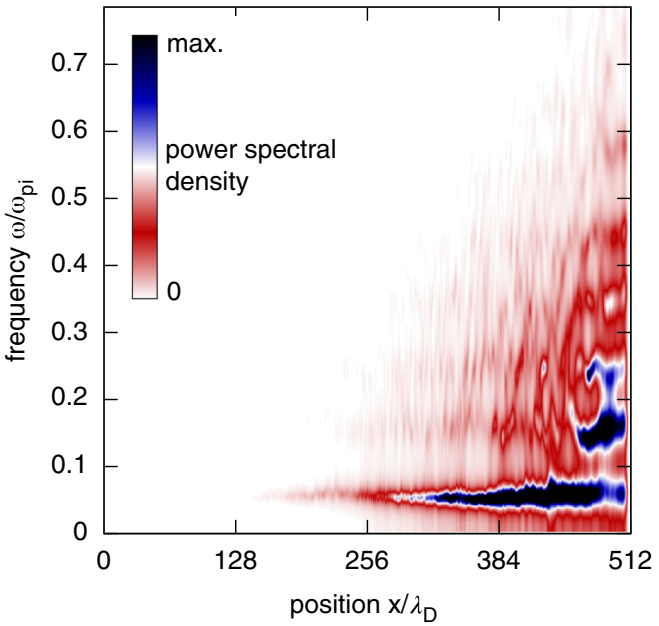

FIG. 3. Power spectral density (psd) vs distance from the center of the discharge and frequency normalized by the ion plasma frequency at the center of the discharge ω_{pi}. A spectral peak with nearly constant frequency which grows with distance from the center of the discharge is found, indicating an unstable acoustic mode.

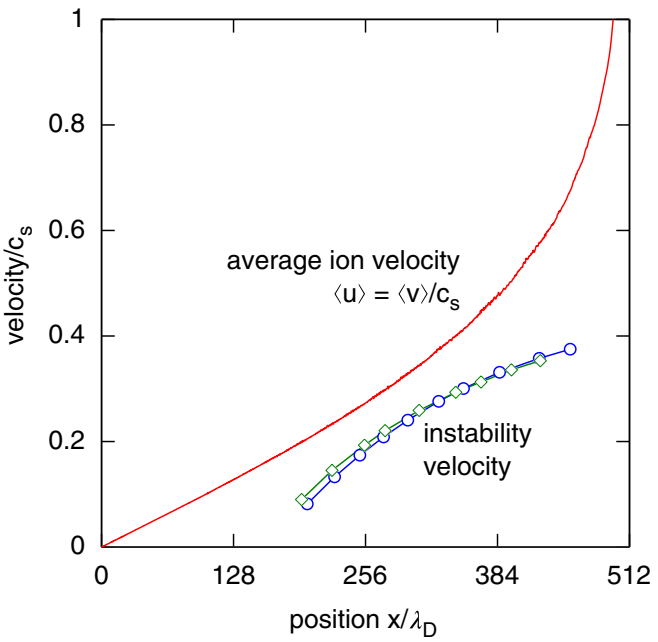

FIG. 5. The speed of unstable acoustic waves vs position x. The average ion velocity $\langle v \rangle / c_s$ is shown for comparison. Speeds are normalized by the ion acoustic speed. The speed of the unstable waves is less than the average ion velocity, indicating that the unstable mode is propagating in the $-x$ direction but is carried to the wall by the ion flow.

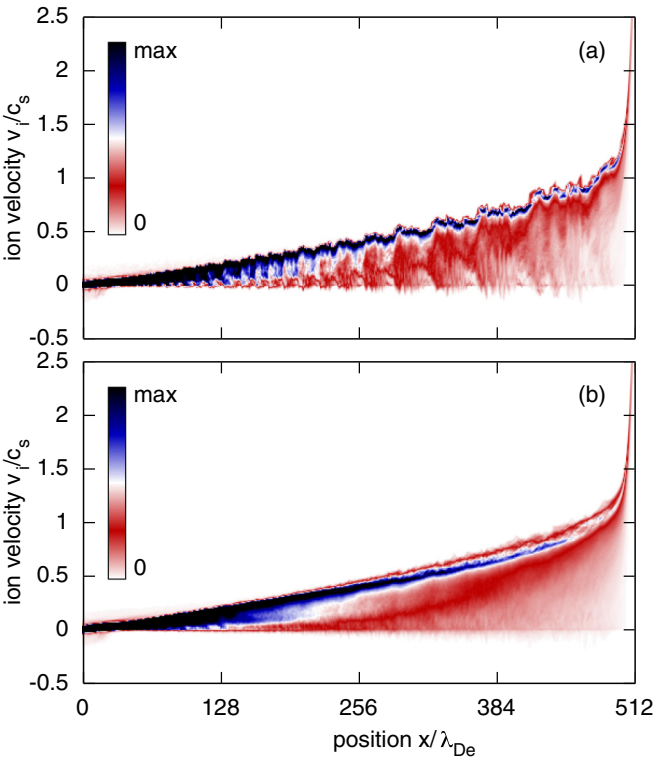

FIG. 4. Time-averaged ion velocity distribution function $f(x,v)$. (a) The average is taken over $13\omega_{pi}^{-1}$ so the effect of the instability on ion trajectories is evident. (b) The average is taken over $128\omega_{pi}^{-1}$, which corresponds roughly to one period of the instability. Note that spatial fluctuations average to nearly zero.

to higher-frequency modes. In Fig. 4(b) we average over a time interval $128\omega_{pi}^{-1}$, which is about one period of the dominant unstable mode. In this case, the spatial fluctuations average nearly to zero, while the temporal fluctuations widen the distribution function in velocity space, leading to a broadening of the steady-state distributions predicted by TL theory [15].

In Fig. 5 we show the dependence of the velocity of the unstable acoustic wave (normalized to the ion acoustic speed) on position and compare it to the average ion speed $\langle v \rangle$. The perturbation velocity is significantly below the ion acoustic speed c_s, which was previously seen qualitatively in Fig. 2. The perturbation velocity is also below the average ion velocity. Consequently, the unstable modes are propagating in the $-x$ direction with speeds less than the average ion velocity and so are convected to the wall by the ion flow. In addition, since they have long wavelengths and their speed in the ion frame is significantly less than c_s, these waves are not described by the standard ion-acoustic dispersion relation.

Root-mean-squared (rms) potential fluctuations $\delta\eta_{rms}$ and the maximum fluctuations $\delta\eta_{max}$ are shown in Fig. 6, where

$$\delta\eta_{rms} = \sqrt{\langle(\eta - \langle\eta\rangle)^2\rangle}. \tag{13}$$

The ratio $\delta\eta_{max}/\delta\eta_{rms}$ is approximately constant, with an average value of 3.4 which is consistent with a Gaussian distribution of fluctuations. There is a small peak near the center of the discharge where short-wavelength ion plasma fluctuations push ions off the potential maximum. The fluctuation level then decreases to the background level until the instability begins to grow at $x/L \approx 0.2$. The growth of the instability is linear (i.e., exponential) in x, where $\delta\eta_{rms} \propto e^{k_i x}$, where $k_i = 0.0094/\lambda_D$

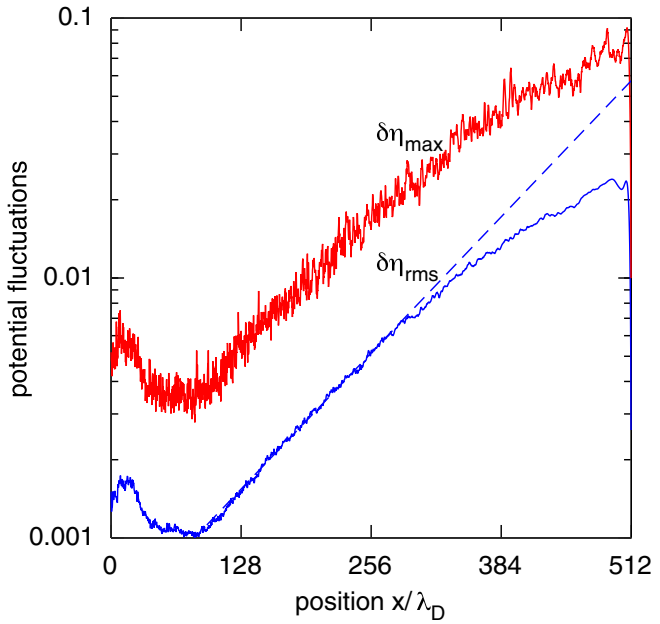

FIG. 6. Root-mean-squared (rms) (blue) and maximum (red) of potential fluctuations. The dashed line gives a linear spatial growth rate of $0.0094/\lambda_D$.

is the spatial growth rate. As discussed above, near the wall the instability saturates at $\delta\eta_{\rm rms} = 0.025$ and $\delta\eta_{\rm max} = 0.09$; i.e., if the electron temperature $T_e = 1$ eV, then the maximum potential fluctuation is $\delta\phi = 0.09$ V.

The effect of varying the system length L is shown in Fig. 7, where we show the $\delta\eta_{\rm rms}$ vs distance from the center of the discharge for $L = 256\lambda_D$, $384\lambda_D$, and $512\lambda_D$. In this case we have rescaled x by L. We find that $\delta\eta_{\rm rms}(x/L)$ is essentially independent of L. This can be explained by recalling that the solution of the cold-source TL model in the plasma limit ($\lambda_D \to 0$) depends only on a single length scale, L_v. Consequently, for the case where the system is a large but finite number of Debye lengths in extent, the system length $L \propto L_v$ is essentially the only length scale and all results in the plasma limit should be self-similar when rescaled by L. This demonstrates that the observed instability scales as we would expect if it is a feature of the time-dependent TL model in the plasma limit. In this case, there is a single universal spatial growth rate, $k_i = 4.8/L$.

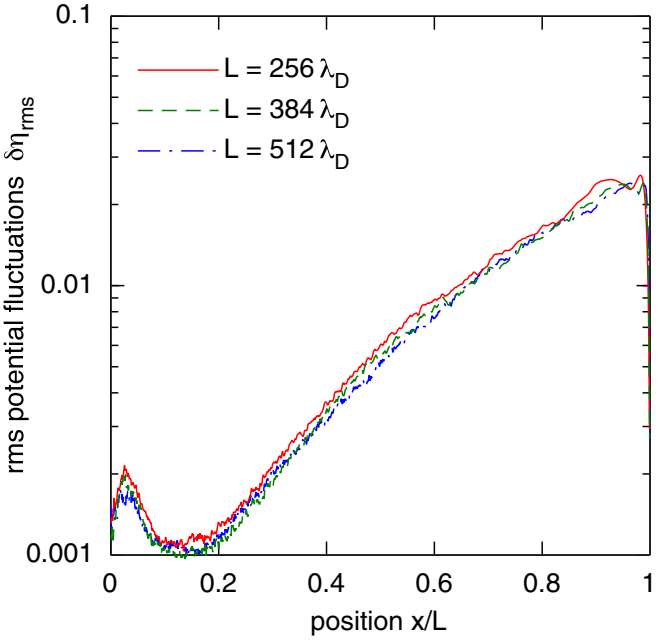

FIG. 7. Root-mean-squared (rms) potential fluctuations vs normalized position x/L for system lengths $L = 256\lambda_D$, $384\lambda_D$ and $512\lambda_D$. The spatial dependence of the fluctuations is effectively independent of L, indicating the fluctuations are a feature of the time-dependent TL model in the plasma approximation $\lambda_D/L \ll 1$.

We investigate the dispersion relations by examining two-dimensional Fourier transforms of the fluctuation data $\delta\eta$ (Fig. 8) in four regions each $128\lambda_D \times 512\omega_{\rm pi}^{-1}$ in size. The transform amplitude will be greatest along the normal modes of the system, which will trace out the branches of the dispersion relation $\omega(k)$, where $k = 2\pi/\lambda$ is the wave number. These are computed in the laboratory frame, and so the plasma flow distorts $\omega(k)$ for both positive and negative wave numbers. Figure 8(a) shows the dispersion relation near the center of the discharge where the ion flow velocity is small. Two distinct wave types are observed. First, there is a standard ion-acoustic wave with an acoustic speed c_s which bends over to the ion plasma frequency $\omega_{\rm pi}$ for large k and which propagates in both the upstream and downstream directions. Second, there are two slow acoustic modes each with a nearly constant speed $\ll c_s$ and which move only in the $+k$ direction. As discussed above, these waves actually propagate in the $-x$ direction but are convected in the $+x$ direction by the ion flow. These are the unstable acoustic modes. As we move towards the wall, the ion flow distorts both the standard acoustic mode and the unstable modes, while an increasing amount of wave energy is concentrated in the unstable modes with more energy at longer wavelengths.

IV. LINEAR INSTABILITY THEORY

The Tonks-Langmuir model consists of the Vlasov-Poisson equations with an ion source and appropriate boundary conditions. As shown in the previous section, numerical solutions demonstrate that the time-dependent TL model has an acoustic-type instability. In this section, we linearize the ion Vlasov-Poisson system, including a zero-order electric field which drives the instability, and derive the linear dielectric function for both general and Maxwellian ion velocity distribution functions. In Sec. V we show that this leads to an instability that matches the observed characteristics seen in the PIC solutions.

The linearized ion Vlasov equation [Eq. (10)] neglecting the source term,

$$\frac{\partial f_1}{dt} + v\frac{\partial f_1}{\partial x} + \frac{e}{M}E_1\frac{\partial f_o}{\partial v} + \frac{e}{M}E_o\frac{\partial f_1}{\partial v} = 0, \qquad (14)$$

can be solved using the method of characteristics. Here, $f_o(x,v)$and $E_o(x)$ are the steady-state velocity distribution function and the electric field, which are assumed to vary on spatial scales much longer than the perturbed quantities $f_1(x,v,t)$ and $E_1(x,t)$. Integrating the equation of motion

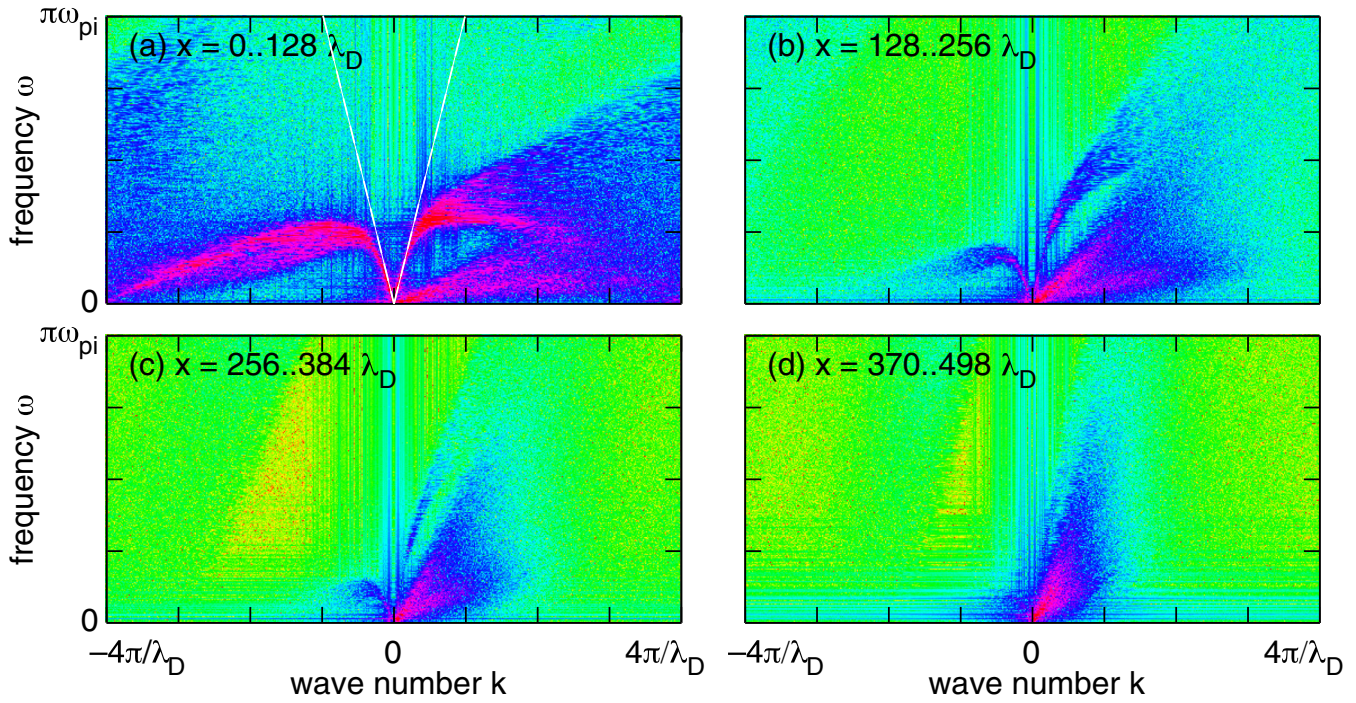

FIG. 8. Average dispersion relations in the laboratory frame found by taking the two-dimensional Fourier transform of the potential fluctuations $\delta\eta$ for regions $128\lambda_D \times 512\omega_{pi}^{-1}$ vs distance from the center of the discharge. For example, in panel (b) the spatial domain extends from $x = 128\lambda_D$ to $256\lambda_D$. The white dashed lines in panel (a) give the ion acoustic speed c_s for a stationary plasma. A standard acoustic wave with the speed c_s is visible together with slow acoustic modes with speeds less than c_s in the laboratory frame which propagate in the $-x$ direction and are carried to the wall by the ion flow.

$Md^2x'/dt'^2 = eE_o$ from time 0 to t subject to the end-point conditions $x'(t' = t) = x$ and $v'(t' = t) = v$ gives

$$f_1(x,v,t) = f_1(x',v',t' = 0) - \frac{e}{M}\frac{\partial f_o}{\partial v}\int_0^t dt'\, E_1(x',t'), \tag{15}$$

where $x' = x - v\tau + \frac{1}{2}(eE_o/M_i)\tau^2$, $v' = v - (eE_o/M)\tau$, and $\tau = t - t'$. Taking the Fourier transform in space and the Laplace transform in time leads to

$$\hat{f}_1(k,v,\omega) = \frac{i\tilde{f}_1(k,v',t' = 0)}{\bar{\omega}_f} - \frac{e}{M}\frac{i\hat{E}_1(k,\omega)}{\bar{\omega}_f}\frac{\partial f_o}{\partial v}, \tag{16}$$

where

$$\frac{1}{\bar{\omega}_f} \equiv -i\int_0^\infty d\tau\, \exp\{i[(\omega - kv)\tau + \alpha_E\tau^2]\} \tag{17}$$

is the inverse frequency response associated with the unperturbed characteristic and

$$\alpha_E \equiv \frac{1}{2}\frac{e}{M}kE_o \tag{18}$$

is an angular acceleration associated with the zero-order electric field.

Calculating the ion density perturbation from $n_{1,i} = \int d^3v f_1$ and inserting the result into the linearized Poisson's equation, $d^2\phi_1/dx^2 = -e(n_{1,i} - n_{1,e})/\epsilon_o$, along with the linear Boltzmann density relation for electrons, $n_{e,1} = n_o e\phi/(k_B T_e)$, leads to the linear dielectric function

$$\hat{\varepsilon}(k,\omega) = 1 + \frac{1}{k^2\lambda_D^2} + \frac{e^2}{\epsilon_o kM}\int dv\,\frac{\partial f_o/\partial v}{\bar{\omega}_f}. \tag{19}$$

Note that the integral in Eq. (17) can be evaluated in terms of tabulated functions: $\bar{\omega}_f^{-1} = \sqrt{\pi}\, w_E \exp(w_E^2)\mathrm{erfc}(w_E)/(\omega - kv)$, where $w_E \equiv \sqrt{-i}(\omega - kv)/(2\sqrt{\alpha_E})$.

A qualitative understanding of the mechanism responsible for the observed TL instability can be obtained by approximating the steady-state ion distribution function as a Maxwellian, $f_M = n_o \exp[-(v - u_i)^2/v_{Ti}^2]/(\sqrt{\pi}v_{\mathrm{Ti}})$, where u_i is the ion flow speed and v_{Ti} is the ion thermal speed. With this, Eq. (19) can be written as

$$\hat{\varepsilon}(k,\omega) = 1 + \frac{1}{k^2\lambda_D^2} - \frac{\omega_{pi}^2/\left(k^2v_{\mathrm{Ti}}^2\right)}{(1 - i\xi_i)}Z'\left[\frac{(\omega - ku_i)/kv_{\mathrm{Ti}}}{\sqrt{1 - i\xi_i}}\right], \tag{20}$$

where Z is the plasma dispersion function [29] and the prime denotes a derivative with respect to the argument. Here,

$$\xi_i \equiv \frac{2ekE/M}{k^2v_{\mathrm{Ti}}^2} = \frac{1}{k\lambda_i} \tag{21}$$

quantifies the influence of the electric field. This can also be described in terms of the length scale $\lambda_i \equiv T_i/(eE)$. In the limit $E \to 0$ the well-known field-free electrostatic dielectric function is returned. A representation of the dielectric function similar to Eq. (20) was first obtained by Fried *et al.* [27]; see also Refs. [30,31].

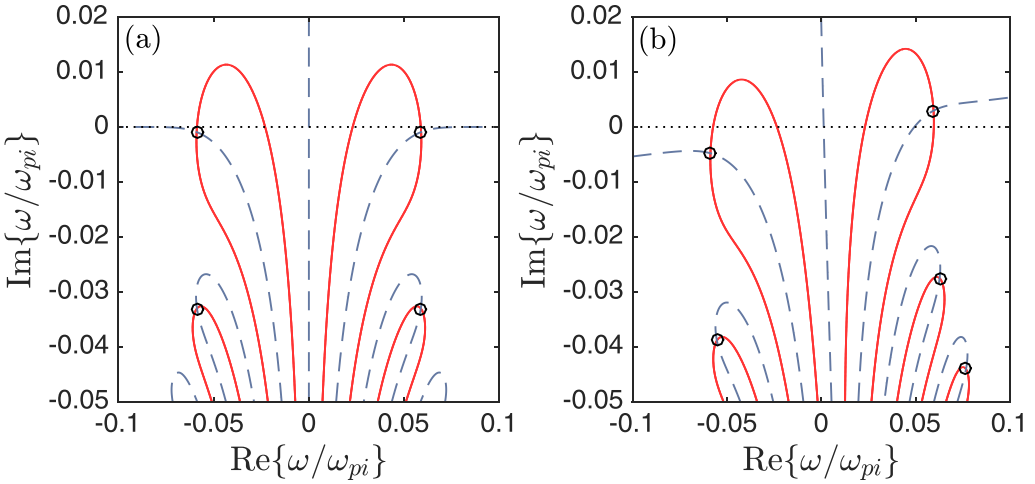

FIG. 9. Roots of the linear dielectric function from Eq. (20) with $k\lambda_D = 0.05$, $T_e/T_i = 10$, and ion flow speed $u_i = 0$: $\mathrm{Re}\{\hat{\varepsilon}\} = 0$ (red solid lines) and $\mathrm{Im}\{\hat{\varepsilon}\} = 0$ (blue dashed lines). Circles are the crossing points, which represent the wave modes. (a) No electric field ($E = 0$) and (b) with the electric field $eE/(T_e/\lambda_D) = -0.001$. The electric field leads to a growing mode.

V. LINEAR INSTABILITY RESULTS

Figure 9 shows that the zero-order electric field rotates the wave mode locations in the frequency phase-space. The lines in the curves represent the solution of Eq. (20) for $\mathrm{Re}\{\hat{\varepsilon}\} = 0$ and $\mathrm{Im}\{\hat{\varepsilon}\} = 0$ for the conditions given in the caption. The crossing points of these lines represent the wave modes. Throughout this section, k is taken to have a positive value and the alignment of the direction of k with reference to the electric field is indicated by the sign of the electric field. It was observed that a positive value of E causes the mode locations to rotate clockwise, and negative values cause them to rotate counterclockwise. For the finite value $eE/(T_e/\lambda_D) = -0.001$ shown, the growth rate of modes with a positive sign of the real frequency increase, and those with negative real frequency decrease, due to E. The single pole in Fig. 9(b) for which $\mathrm{Im}\{\omega\} > 0$ indicates a linearly unstable mode which propagates only in the direction opposite E in the ion frame.

The growth rate of this instability is found to increase with the electric field strength and to be peaked at a wavelength that is significantly longer than the electron Debye length. The real frequency corresponding to the maximum growth rate is approximately an order of magnitude lower than the ion plasma frequency. Figure 10 shows the dispersion relation computed from Eq. (20) for five values of the electric field strength $eE/(T_e/\lambda_D) = 0$, -0.0001, -0.0005, -0.001, and -0.005. These values are typical of those in steady-state TL solutions. For small electric fields there is a wide range of unstable wave numbers with similar small growth rates. For stronger electric fields the growth rate peaks at shorter wavelengths. The real frequency is observed to deviate from the standard acoustic solutions with a phase velocity c_s [Fig. 10(b), black line] at long wavelengths.

For weak electric fields, only long wavelength modes are predicted to be unstable, and the growth rate is small. For these modes in particular, it is instructive to consider the fundamental scale separation condition underlying linear theory: that the wavelengths ($\lambda = 2\pi/k$) be much shorter than the gradient scale L_E of the background. Since the electric

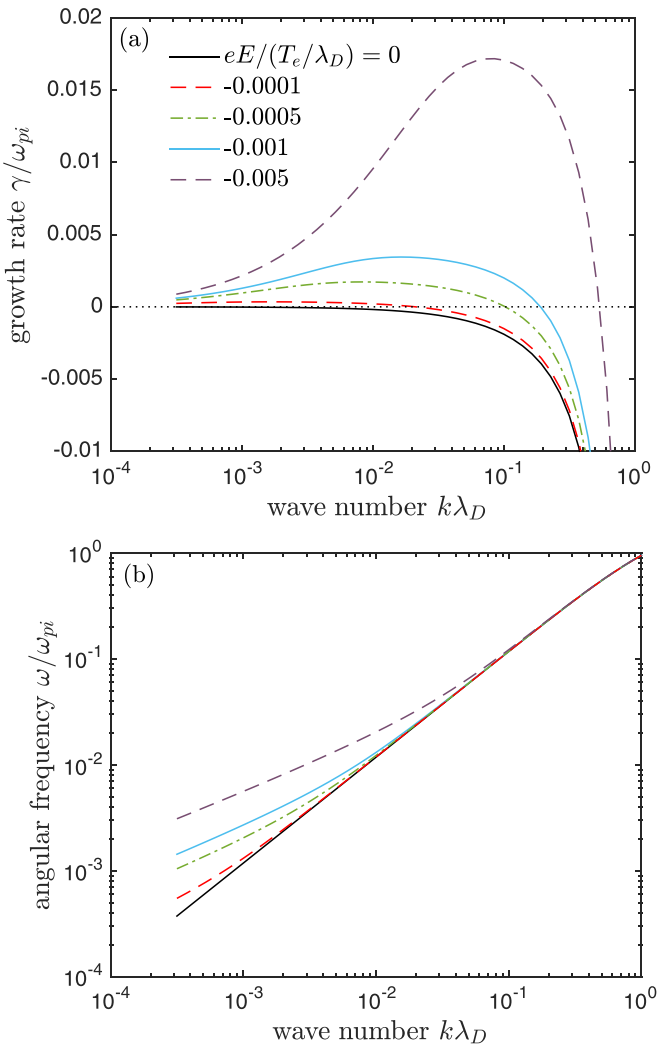

FIG. 10. (a) Growth rate and (b) real angular frequency of the linear dispersion relation computed from Eq. (20). The common data in each curve was $T_e/T_i = 10$ and ion flow speed $u_i = 0$. The five chosen values of the electric field are indicated in the legend.

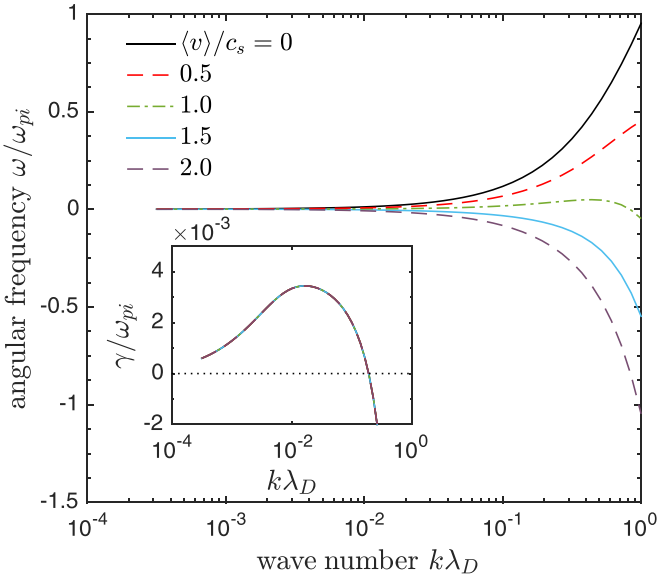

FIG. 11. Angular frequency and growth rate (inset) vs wave number for the linear dispersion relation computed from Eq. (20) with $T_e/T_i = 10$ and $eE/(T_e/\lambda_D) = -0.001$ at the five values of u_i/c_s indicted in the legend. All five curves are shown for the growth rate, but are indistinguishable, demonstrating that the growth rate is independent of the average ion velocity.

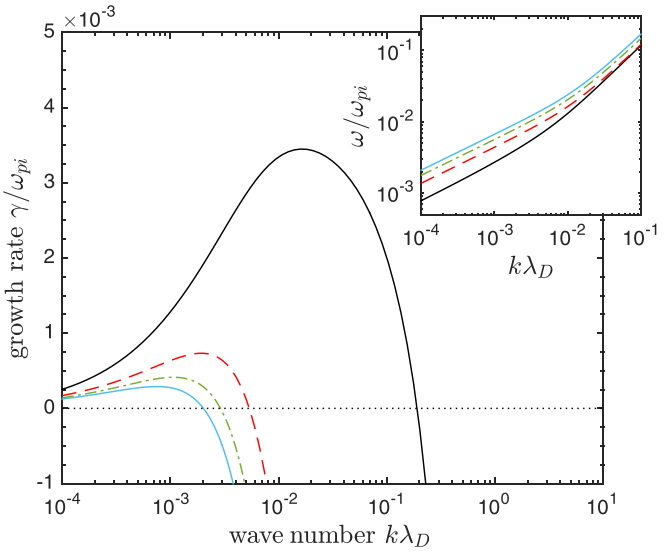

FIG. 12. Growth rate and angular frequency (inset) of the linear dispersion relation computed from Eq. (20) for $T_e/T_i = 10$, $eE/(T_e/\lambda_D) = -0.001$, and $\langle v\rangle/c_s = 0$ for four distinct wave modes.

field is the only steady-state field in this case, L_E is estimated based on the gradient scale of the electrostatic potential $L_E \simeq T_e/|eE|$, where T_e indicates a characteristic value of the electric potential, referenced to the center of the discharge, in the region of interest. Taking the $eE/(T_e/\lambda_D) = -0.001$ case as an example, the shortest wavelength of the unstable modes is approximately $30\lambda_D$, whereas $L_E \simeq 1000\lambda_D$. For these modes, the assumed scale separation is well satisfied. However, the assumption can be violated for very long wavelengths ($k\lambda_D \lesssim 0.01$) as shown in Fig. 10.

The electric field drive mechanism for this instability is fundamentally different than the familiar ion-acoustic instability. This is emphasized in Fig. 11, which shows that the growth rate of the instability does not depend on the ion flow speed u_i. Here, five u_i values ranging from 0 to $-2c_s$ are shown; negative values correspond to the TL model situation where the ion flow is in the same direction as the electric field ($-\hat{k}$ in this case). Each of the growth rate curves here is indistinguishable. In contrast, ion acoustic instabilities are driven by the relative drift between electrons and ions and highly influenced by the value of u_i [25]. The standard ion-acoustic instability is not possible in the model of Eq. (20) because it requires a differential flow between two plasma components. The only influence ion flow has on the observed instability is to Doppler shift the real mode frequency in the laboratory frame.

A further observation distinguishing this instability from more familiar types is that multiple wave modes with different wave velocities may be unstable. Figure 12 shows an example of four such unstable modes. These modes correspond to the positive real frequency modes shown in Fig. 9. Although only one of the modes shown in this figure has a positive growth rate at $k\lambda_D = 0.05$, the parameter determining the magnitude of the rotation in the frequency phase-space is $\xi_i = eE/(kT_i)$; either increasing E or decreasing k increases the rotation. For sufficiently small k, multiple modes can have a positive growth rate, as shown in the dispersion relation in Fig. 12. However, the scale separation assumed for the linearization breaks down at these long wavelengths. In this context, it is also worth noting that these normally damped modes represent kinetic modes, which are known to be the branches through which nonlinear transfer of energy occurs [32,33].

Figure 13 shows the predicted linear growth rate for parameters obtained from solutions of the steady-state cold TL model. The electric field, density, average ion speed, and rms ion speed were obtained from the analytical expressions for steady-state solutions of the TL model in Refs. [4] and [15] and are shown in panel Fig. 13(a). The linear dispersion relation was computed at each point along the profile using Eq. (20) with values for the density, average ion speed, and effective ion temperature ($T_e/T_i = 2/u_{\rm rms}^2$) from the cold TL model. The linear dielectric function from Eq. (20) assumes that the distribution is Maxwellian, which differs from the highly non-Maxwellian TL distribution, so the results obtained in this way are an approximate, rather than an exact, evaluation of the linearized cold TL theory.

Figure 13(b) shows the maximum growth rate vs position. It is observed to be largest near the sheath, but also larger near the center of the discharge where the instability begins growing. Although the electric field is weaker toward the center, T_e/T_i is largest there. Data are omitted for $x/L \lesssim 0.2$ because in this region the ion temperature in the cold TL model becomes unphysically small, indicating that finite ion source temperature effects are important. Moving from the center toward the sheath, the growth rate decreases, presumably due to the increase in T_i having a comparatively more significant influence on the growth rate than the slight increase of E. Close to the sheath edge, the larger electric field leads to a substantial rise in the peak growth rate. Figures 13(c) and 13(d) show the

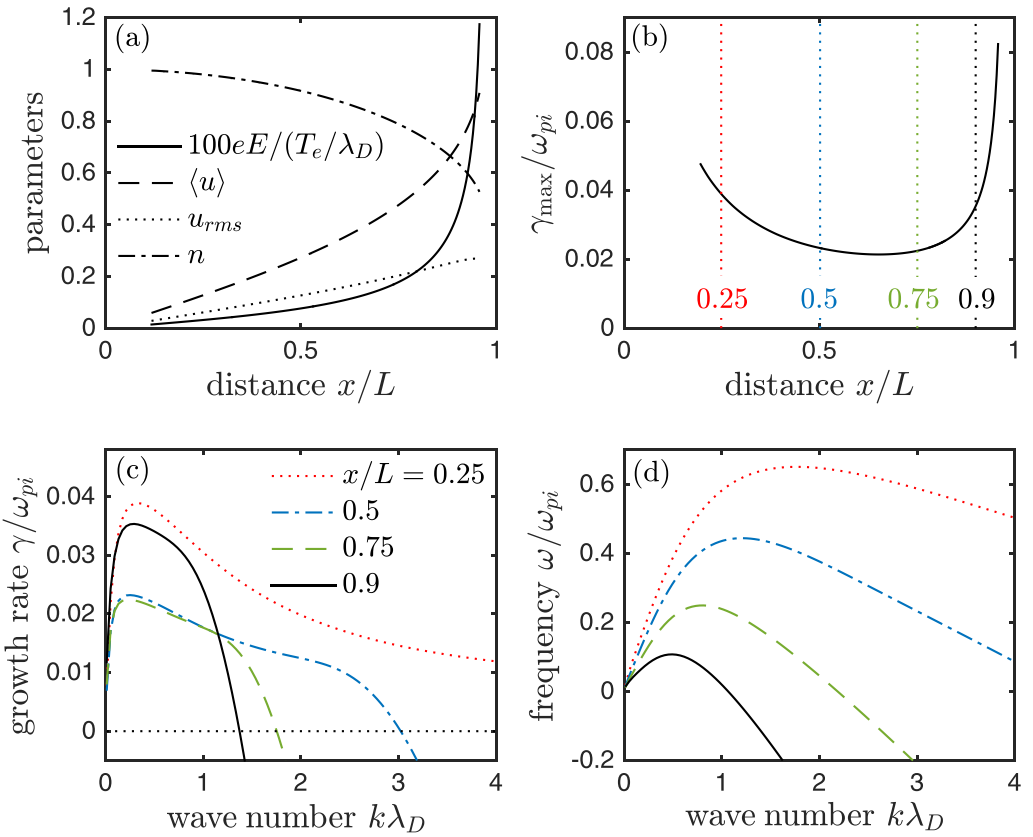

FIG. 13. (a) Profiles of electric field (solid line), ion flow speed (dashed line), rms ion speed (dotted line) and density (dash-dotted line) from the steady-state TL model (Ref. [15]). (b) The computed maximum linear growth rate computed from Eq. (20) using the parameters from panel (a). (c) Growth rate and (d) real frequency of the instability at the four spatial locations indicated in the legend.

growth rate and the real angular frequency of the instability at four locations. These show that for $x/L = 0.25$, close to where the instability begins growing, there is a well-defined peak in the growth rate which fixes the instability frequency and wavelength—the most unstable wavelengthis $\sim 10\lambda_D$ and the corresponding real frequency $\omega \approx 0.1\omega_{\rm pi}$. Both of these predictions are in qualitative agreement with the numerical solutions. In particular, the instability begins to grow near the center of the discharge with a well-defined frequency and initial wavelength. As the wave propagates to the wall, the wave speed in the laboratory frame increases and the wavelength must increase to keep the frequency constant.

VI. CONCLUSIONS

We have solved the time-dependent extension of the Tonks-Langmuir model [1,2,4,15] computationally. We observe standard ion-acoustic waves which are created near the sheath-plasma boundary and propagate across the discharge at the ion acoustic speed c_s. Significantly, we also observe unstable acoustic modes that begin growing near the center of the system and saturate near the sheath-plasma boundary. The unstable modes have frequencies well below the ion plasma frequency and wavelengths which increase from $\sim 7\lambda_D$–$10\lambda_D$ near the discharge center to $\sim 40\lambda_D$–$50\lambda_D$ near the discharge walls. The root-mean-squared fluctuation amplitude $\delta\phi_{\rm rms} \approx 0.025kT_e/e$, where T_e is the electron temperature, or the maximum fluctuation $\delta\phi \approx 0.09k_BT_e/e$ or about 10% of the electron temperature in electron volts. An analysis of the linearized Vlasov-Poisson system indicates that the instability corresponds to slow acoustic modes which are destabilized by the zero-order electric field and which are convected to the walls by the ion flow. In particular, the instability begins to grow around $x/L \approx 0.2$, where L is the distance from the center of the discharge to the wall. The frequency is set at this point, and the wavelength increases and the wavelength and the wave velocity in the laboratory frame increase as the unstable modes move to the wall.

ACKNOWLEDGMENT

One of the authors (S.D.B.) was supported by DOE Grant Award No. DE-SC0016473.

[1] L. Tonks and I. Langmuir, Phys. Rev. **34**, 876 (1929).

[2] E. R. Harrison and W. B. Thompson, Proc. Phys. Soc. **74**, 145 (1959).

[3] A. Caruso and A. Cavaliere, Nuovo Cimento **26**, 1389 (1962).
[4] S. A. Self, Phys. Fluids **6**, 1762 (1963).
[5] M. J. Goeckner, J. Goree, and T. E. Sheridan, Phys. Fluids B **4**, 1663 (1992).
[6] G. Bachet, L. Chérigier, M. Carrère, and F. Doveil, Phys. Fluids B **5**, 3097 (1993).
[7] G. Bachet, L. Chérigier, and F. Doveil, Phys. Plasmas **2**, 1782 (1995).
[8] N. Claire, G. Bachet, U. Stroth, and F. Doveil, Phys. Plasmas **13**, 062103 (2006).
[9] G. A. Emmert, R. M. Wieland, A. T. Mense, and J. N. Davidson, Phys. Fluids **23**, 803 (1980).
[10] R. C. Bissell and P. C. Johnson, Phys. Fluids **30**, 779 (1987).
[11] J. T. Scheuer and G. A. Emmert, Phys. Fluids **31**, 1748 (1988); **31**, 3645 (1988).
[12] R. J. Procassini, C. K. Birdsall, and E. C. Morse, Phys. Fluids B **2**, 3191 (1990).
[13] H.-P. van den Berg, K.-U. Riemann, and G. Ecker, Phys. Fluids B **3**, 838 (1991).
[14] K.-U. Riemann, Phys. Fluids **24**, 2163 (1981).
[15] T. E. Sheridan, Phys. Plasmas **8**, 4240 (2001).
[16] S. Robertson, Phys. Plasmas **16**, 103503 (2009).
[17] D. D. Tskhakaya Sr., L. Kos, and N. Jelić, Phys. Plasmas **21**, 073503 (2014).
[18] K. Sato and F. Miyawaki, Phys. Fluids B **4**, 1247 (1992).
[19] V. A. Godyak, V. P. Meytlis, and H. R. Strauss, IEEE Trans. Plasma Sci. **23**, 728 (1995).
[20] T. E. Sheridan, N. St. J. Braithwaite, and R. W. Boswell, Phys. Plasmas **6**, 4375 (1999).
[21] S. D. Baalrud and C. C. Hegna, Plasma Sources Sci. Technol. **20**, 025013 (2011).
[22] C.-S. Yip, N. Hershkowitz, and G. Severn, Plasma Sources Sci. Technol. **24**, 015018 (2015).
[23] S. D. Baalrud, C. C. Hegna, and J. D. Callen, Phys. Rev. Lett. **103**, 205002 (2009).
[24] C.-S. Yip, N. Hershkowitz, and G. Severn, Phys. Rev. Lett. **104**, 225003 (2010).
[25] S. D. Baalrud, Plasma Sources Sci. Technol. **25**, 025008 (2016).
[26] D. D. Tskhakaya Sr., L. Kos, and D. Tskhakaya, Phys. Plasmas **23**, 032128 (2016).
[27] B. D. Fried, M. Gell-Mann, J. D. Jackson, and H. W. Wyld, J. Nucl. Energy, Part C: Plasma Phys. **1**, 190 (1960).
[28] C. K. Birdsall and A. B. Langdon, *Plasma Physics via Computer Simulation* (Hilger, Bristol, 1991), p. 393.
[29] B. D. Fried and S. C. Conte, *The Plasma Dispersion Function* (Academic, New York, 1961).
[30] B. D. Fried and G. J. Culler, Phys. Fluids **6**, 1128 (1963).
[31] G. F. Reiter, Phys. Fluids **10**, 703 (1967).
[32] F. Skiff, S. De Souza-Machado, W. A. Noonan, A. Case, and T. N. Good, Phys. Rev. Lett. **81**, 5820 (1998).
[33] D. R. Hatch, P. W. Terry, F. Jenko, F. Merz, M. J. Pueschel, W. M. Nevins, and E. Wang, Phys. Plasmas **18**, 055706 (2011).